Nanoscale

On the optical anisotropy in 2D metal-halide perovskites

Journal:	*Nanoscale*
Manuscript ID	NR-ART-10-2021-006899.R1
Article Type:	Paper
Date Submitted by the Author:	22-Nov-2021
Complete List of Authors:	Steger, Mark; National Renewable Energy Laboratory, Janke, Svenja; Duke University, Thomas Lord Department of Mechanical Engineering and Materials Science; University of Warwick, The Institute of Advanced Study; University of Warwick, Department of Chemistry Sercel, Peter; Center for Hybrid Organic Inorganic Semiconductors for Energy, ; Peter Sercel Research,LLC, Larson, Bryon; National Renewable Energy Laboratory Lu, Haipeng; The Hong Kong University of Science and Technology, Chemistry; National Renewable Energy Laboratory Qin, Xixi; Duke University, Thomas Lord Department of Mechanical Engineering and Materials Science Yu, Victor Wen-Zhe; Duke University, Thomas Lord Department of Mechanical Engineering and Materials Science Blum, Volker; Duke University, Thomas Lord Department of Mechanical Engineering and Materials Science; Duke University, Department of Chemistry Blackburn, Jeffrey; National Renewable Energy Laboratory

On the optical anisotropy in 2D metal-halide perovskites

Mark Steger,[1,,#] Svenja M. Janke,[2,3,4,#] Peter C. Sercel,[5,#] Bryon W. Larson,[1] Haipeng Lu,[1,6] Xixi Qin,[2] Victor Wen-zhe Yu,[2] Volker Blum,[2,7] Jeffrey L. Blackburn[1,*]*

1. National Renewable Energy Laboratory, Golden, CO 80401
2. Thomas Lord Department of Mechanical Engineering and Materials Science, Duke University, Durham, NC 27708
3. The Institute of Advanced Study, University of Warwick, CV4 7AL Coventry, United Kingdom
4. Department of Chemistry, University of Warwick, Coventry, CV4 7AL, United Kingdom
5. Center for Hybrid Organic Inorganic Semiconductors for Energy, Golden, CO, 80401 USA
6. Department of Chemistry, The Hong Kong University of Science and Technology, Clear Water Bay, Hong Kong
7. Department of Chemistry, Duke University, Durham, NC 27708

\# Equal Contributions

* Corresponding Author E-mails: mark.steger@nrel.gov ; Jeffrey.blackburn@nrel.gov

Abstract

Two-dimensional metal-halide perovskites (MHPs) are versatile solution-processed organic/inorganic quantum wells where the structural anisotropy creates profound anisotropy in their electronic and excitonic properties and associated optical constants. We here employ a wholistic framework, based on semiempirical modeling (k·p calculations) informed by hybrid density functional theory (DFT) and multimodal spectroscopic ellipsometry on (C6H5(CH2)2NH3)2PbI4 films and crystals, that allows us to link the observed optical properties and anisotropy precisely to the underlying physical parameters that shape the electronic structure of a layered MHP. We find substantial frequency-dependent anisotropy in the optical constants and close correspondence between experiment and theory, demonstrating a high degree of in-plane alignment of the two-dimensional planes in both spin-coated thin films and cleaved single crystals made in this study. Hybrid DFT results elucidate the degree to which organic and inorganic frontier orbitals contribute to optical transitions polarized along a particular axis. The combined experimental and theoretical approach enables us to estimate the fundamental electronic bandgap of 2.65 – 2.68 eV in this prototypical 2D perovskite and to determine the spin-orbit coupling ($\Delta_{SO} = 1.20$ eV) and effective crystal field ($\delta = -1.36$ eV) which break the degeneracy of the frontier conduction band states and determine the exciton fine structure. The methods and results described here afford a better understanding of the connection between structure and induced optical anisotropy in quantum-confined MHPs, an important structure-property relationship for optoelectronic applications and devices.

Introduction

Hybrid organic-inorganic perovskites, especially metal halide perovskites (MHPs), have emerged as attractive semiconductors for a wide range of applications, including photovoltaics [1–3], solid-state lighting [4,5], photocatalysis [6], and information processing [7]. MHPs that are quantum confined in one or more dimensions have strong and tunable absorption and emission spectra that are beneficial for solution-processed optoelectronic applications [8,9]. Relative to 'bulk' three-dimensional perovskites, two-dimensional (2D) MHPs, such as the prototypical $(C_6H_5(CH_2)_2NH_3)_2PbI_4$ (2-**p**henyl**e**thylammonium lead (**P**b) **i**odide, PEPI), can be viewed as solution-processed quantum wells (QWs) with large exciton binding energies, anisotropic carrier/exciton transport, and enhanced environmental and operational stability [10,11]. In recent years, the fundamental properties of charge carriers, excitons, and spin populations in 2D MHPs have been studied extensively as these technologically emergent materials have inspired a variety of optoelectronic applications [12–16]. Accurate knowledge of a semiconductor's optical constants is critical for rational incorporation into optoelectronic devices. As examples, frequency-dependent optical constants are used to model the spatial modulation of optical fields in solar cells [17] and light-emitting diodes (LEDs) [18] and can also be used to estimate important properties such as the exciton binding energy.

The solution-phase precursors for 2D MHPs self-assemble into monolayer sheets of lead-iodide octahedra separated by organic ligand spacers (Figure 1). The insulating ligands act as electronic barriers for electrons and holes, creating a natural quantum well. Being comprised of such distinct molecular environments, these quantum wells were shown to exhibit *dielectric confinement*, which greatly increases the exciton binding energy over the theoretical contribution from quantum confinement alone (as dominates in traditional III-V QWs) [19].

The low-symmetry structure of 2D MHPs (e.g. PEPI) should naturally result in strong optical anisotropy, as has been observed for other 2D semiconductors such as monolayer transition metal dichalcogenides (TMDCs) [20] and epitaxially grown (e.g. III-V and II-VI) QWs [21]. This anisotropy should be especially strong for quantum-confined excitons in the lead-iodide sheets since the spatial distortion of the electron and hole wavefunctions greatly modifies the angular dependence of the dipole moment. Accordingly, recent experimental studies have identified the angular-polarization dependence of the exciton oscillator strength [22], optical constants [23,24], and the resulting photoluminescence (PL) efficiency [25] in PEPI and related 2D perovskites. Optical anisotropy has already been theoretically seen for other 2D hybrid perovskites besides PEPI [26,27]. However, a complete analysis of optical anisotropy in the prototypical 2D hybrid perovskite PEPI, combining experiment and computation to trace the electronic origins of single-particle transitions and excitonic effects, is to the best of our knowledge still missing.

Here, we leverage a combination of multimodal ellipsometry, density functional theory (DFT) calculations, and multi-band K.P/ effective mass theory to demonstrate and characterize strong anisotropy of the optical transitions in PEPI as a model 2D MHP semiconductor. Our experimental analysis couples absorbance spectroscopy with reflection mode and transmission mode ellipsometry to reduce correlations between the anisotropic optical constants of the material. We probe both spin-coated thin films and exfoliated single crystals to quantify birefringence in the near-infrared, dichroism in the visible and UV regions of the spectrum, and strong optical anisotropy of the dominant excitonic transition. This detailed experimental analysis is coupled with an in-depth first-principles based computational analysis that employs all-electron, semilocal and hybrid DFT (HSE06 [28]) including spin-orbit coupling (SOC) effects (implemented in the FHI-aims code [29–31]; for details see below) to obtain the independent-particle electronic structure and corresponding calculated, direction-resolved dielectric function. Next, in order to capture excitonic contributions, we add multiband K.P theory in conjunction with an effective mass description of the excitonic states to relate the DFT results to the excitonic dielectric response.

The theoretical results confirm the directionally-dependent critical points in the highly anisotropic PEPI. We find good agreement between the calculated near-bandgap dielectric response and the experimentally observed anisotropic exciton oscillator strengths. Importantly, the combination of ellipsometry, high-level DFT and multiband K.P/effective mass theory allows us to pinpoint a precise value for the fundamental (electronic) bandgap in PEPI, i.e., 2.65-2.68 eV and to determine the origin and magnitude of the effective crystal field [32] and the spin orbit coupling responsible for the anisotropy of the intrinsic oscillator strength associated with polarization perpendicular versus parallel to the lead-halide sheets. The fundamental gap is an important semiconductor parameter but, as we summarize below, the existing literature did not agree on a specific value. The combination of methods employed in this paper resolves this issue. The theoretical calculations also help to corroborate our remarkable observation that rapidly spin-coated thin films produce exceptional in-plane alignment that is comparable to slowly grown self-assembled crystals. *Our results, which are generalizable to 2D MHPs and even other low-dimensional semiconductors, demonstrate that careful application of ellipsometry can provide a valuable connection* *between the* ***intrinsic optical properties*** *of an ideal material with the* ***realized structure*** *in crystals and partially ordered films.*

Results:

Multi-modal Ellipsometry of PEPI Samples with Varying Structural Order and Alignment

Here, we use spectroscopic ellipsometry to analyze optical anisotropy in $(C_6H_5(CH_2)_2NH_3)_2PbI_4$ (PEPI) as a model 2D MHP quantum well. As shown in Figure 1a, 2D sheets of PbI_4 octahedra project along equivalent ***b*** and ***c*** axes, defining an x-y plane that is structurally distinct from the ***a*** crystal axis (z direction). Based on the *structural* anisotropy of this system, we expect strong optical anisotropy. We prepare PEPI as either spin-coated thin films or thin crystals that are mechanically cleaved from bulk crystals. We find that the spin coated material is very well optically ordered, showing identical magnitude of birefringence in the IR as the crystal and very similar dichroism at the prominent exciton mode, discussed in detail later.

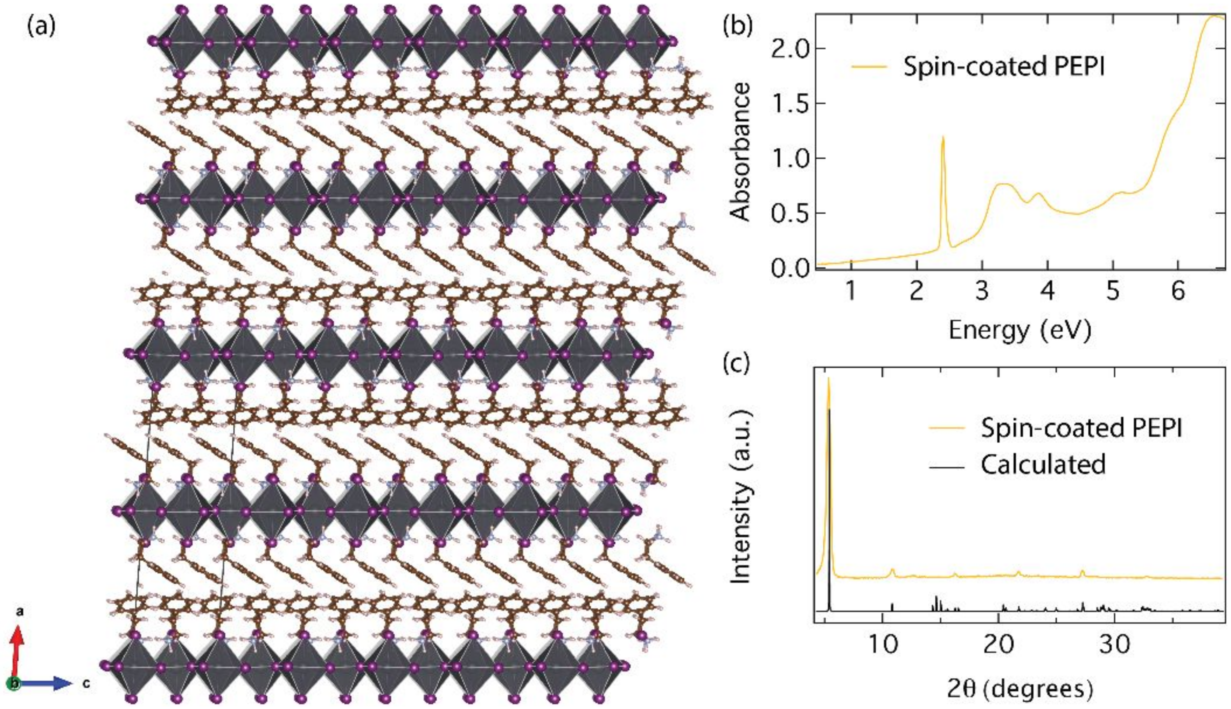

Figure 1: (a) Atomic structure of PEPI, including the outline of the double-layer vertical unit cell used in the DFT computations in this work. ***a***-direction is almost perpendicular to the organic and inorganic plane. (b) absorbance (ABS) of an 80-nm thin film of PEPI on fused silica. (c) Experimental XRD pattern of an 80 nm thick PEPI thin film (orange trace). Black trace shows the XRD pattern simulated single-crystal XRD nuclear coordinates.

Figure 1b shows the optical absorbance of a PEPI thin film (ca. 80 nm thick) on a quartz substrate. The absorbance is dominated by a strong and relatively narrow (ca. 170 meV) exciton resonance centered at 2.4 eV, and multiple additional peaks can be observed into the ultraviolet (UV) region. The experimental thin-film x-ray diffraction (XRD) pattern (orange trace, Fig. 1c) demonstrates a sharp (002) diffraction peak at $2\theta = 5.4°$, corresponding to the 16.35 Å separation between ordered PbI_4 planes. The strong (002) diffraction peak and the close match of the experimental thin-film pattern to the pattern simulated from single-crystal XRD nuclear coordinates (black trace) are consistent with a high degree of purity for the n=1 (i.e. single inorganic layers separated by organic layers) 2D phase and a high degree of ordering within the thin film parallel to the substrate.

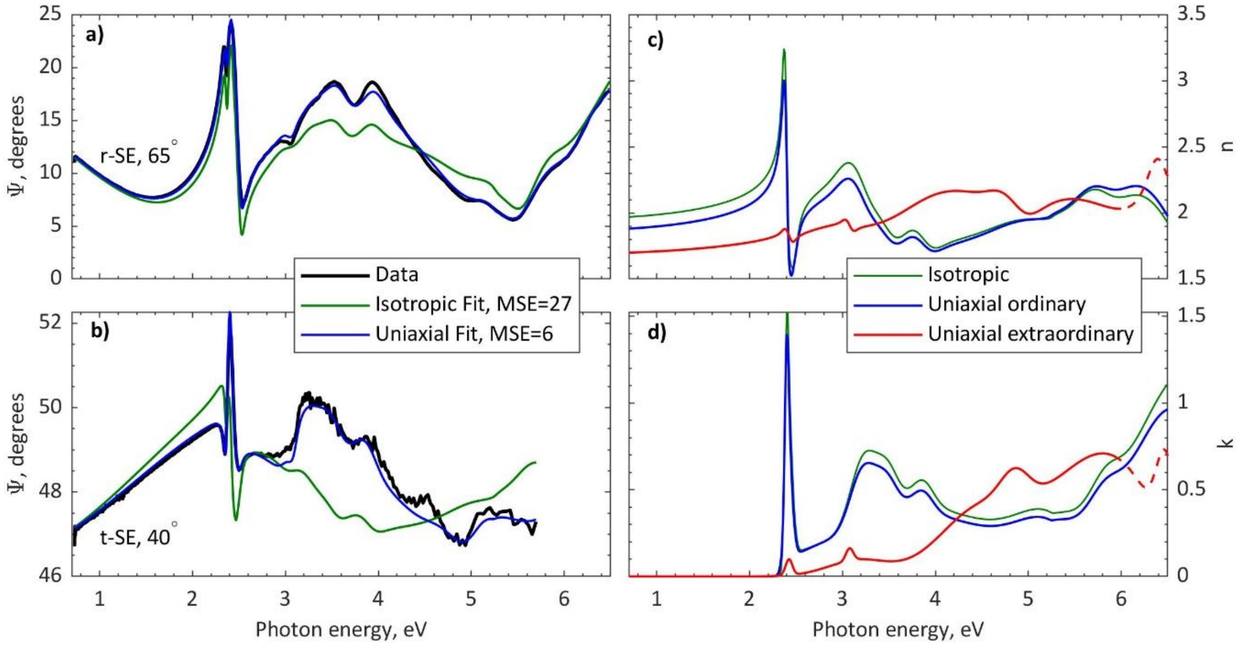

Figure 2: Multimodal ellipsometric analysis of spin coated PEPI thin films. Representative rSE (a) and tSE (b) experimental data (black line) at specified angles, along with isotropic (green line) and uniaxial anisotropic (blue line) fits. Although not shown here, rSE and tSE are taken from 45° to 75° and 0° to 70°, respectively, and transmittance (Fig 1b) is fit simultaneously with rSE and tSE. (c) and (d) The resulting optical models for n (c) and k (d) from the isotropic and uniaxial anisotropic fits. The strong birefringence of PEPI is found to be Δn=-0.18 in the infrared ($E_{ph} <$ 1 eV) . Dashed extraordinary model above 6 eV highlights our reduced sensitivity because of lack of tSE data.

Spin-coated PEPI thin films are measured by transmittance, reflection ellipsometry (rSE) and transmission ellipsometry (tSE). Figures 2a and 2b show representative fits to rSE and tSE Ψ data (black lines) for an 80 nm spin-coated PEPI film on quartz assuming isotropic (green line) or uniaxial anisotropic (blue line) models. The three datasets are fit simultaneously and self-consistently (see Supporting Information (SI), section S1) to maximize sensitivity to the in-plane and out-of-plane optical constants for the film. While rSE gives very high sensitivity to in-plane optical constants, surface roughness and layer thickness, cross-correlations with extraordinary optical constants can greatly degrade model parameter confidence intervals. Inclusion of tSE greatly improves sensitivity to the out-of-plane optical constants by reducing cross-correlations with the ordinary axis *n* and *k* [18]. Similarly, normal-incidence transmittance improves sensitivity to in-plane absorption and reduces the cross-correlation between thickness and k [33]. We find that the standard error of the fit (MSE) is significantly worse for the isotropic fit compared to the anisotropic fit. Figure 2a and b show that the isotropic fit (green lines, MSE = 27) also fails to qualitatively reproduce the experimental data (black line). In contrast, the anisotropic fit (blue line, MSE = 6) reproduces the experimental behavior well.

We further improve the models by analyzing multiple samples of different thicknesses and converting the B-spline model into a general oscillator model to interpret confidence on the critical point features (see Methods and SI section S1). Figures 2c and d show the optical constants *n* and *k*, respectively, for the resulting isotropic and anisotropic models. Due to insufficient transmission through the films at high photon energy, we truncate tSE analysis above 6 eV and therefore the confidence on the extraordinary optical constants is reduced in this range (dashed lines, Fig. 2c and 2d). Analysis of the in-plane (ordinary) and out-of-plane (extraordinary) refractive indices demonstrates that this PEPI thin film is strongly anisotropic, exhibiting a large birefringence: Δn=-0.18 at 1500 nm to more than Δn=-0.3 at 600 nm. The analysis also demonstrates that applying an isotropic model to anisotropic media can result in dramatic errors, even in the transparent region. In this case, the refractive index derived from the isotropic model is 4% larger than that of the ordinary axis *n* and 15% larger than that of the extraordinary axis, rather than falling between the ordinary and extraordinary optical constants. This significant error in *n* would propagate to erroneous thickness estimates and quantum yield calculations. The poor quality of isotropic ellipsometric fits would furthermore hamper any attempts at deeper characterization of film quality (e.g. porosity and surface quality) as well as frequency-dependent optical modeling of device stacks in e.g. solar cells or LEDs.

In spite of the rapid spin-coating preparation, the PEPI thin film has pronounced dichroism throughout the absorbing region, indicating a noticeable degree of order in the film. For example, ordinary axis absorption dominates the transitions below 4 eV, while extraordinary-axis absorption becomes stronger above 4 eV and shows peaks that do not appear in the ordinary axis absorption. This contrasts with spin-coated polymers, which often exhibit uniaxial anisotropy in the extent to which the critical points manifest in-plane or out of plane due to incomplete alignment of molecules in the film [34], while here the critical points appear at different energies in either axis. Also, while the predominant oscillator strength of the excitonic peak (2.4 eV) is in the plane of the film (ordinary axis), the peak also appears to have a small amount of oscillator strength in the extraordinary axis. It seems sensible to conclude that the strong spectral variation in the ordinary and extraordinary optical constants is connected to structural order of the inorganic and organic sub-lattices within the thin film and the contribution of specific organic and/or inorganic orbitals to particular optical transitions. We explore this connection in detail below, using DFT calculations in conjunction with multiband k·p calculations and an effective mass description of the excitons.

To delve deeper into the optical response of highly ordered PEPI, we explore crystals grown by slow crystallization from saturated precursor solutions (see methods). Bulk crystals of 2D MHPs are expected to represent a model system for highly aligned 2D planes *if* the crystal registry is retained over length scales probed by the ellipsometry measurement. Experimentally, we find that the surface of as-grown ‘bulk’ crystals is rough and disordered (Fig. 3a, b), due to the presence of different single-crystal grains of varying orientation. As such, these bulk crystals are too disordered to recover reliable data from rSE measurements and are also too thick to observe and model back-surface reflections in the non-absorbing region below the optical bandgap. To achieve clean surfaces and thinner crystals with sufficient long-range order over the area of the focused ellipsometry probe beam (dashed red line, Fig. 3c), we exfoliate crystals on the order of 1-10 microns thick using a heat release tape (Fig. 3c) [35]. The resulting crystals are investigated solely with rSE, due to insufficient transmission through the thick crystals in the visible region. Single crystal x-ray diffraction confirmed that these smooth-faced crystals are an identical match to literature x-ray structure for PEPI and the starting structure used in our theory (see SI section S2).

Representative Ψ data (black traces) and fits (red traces) for two separate cleaved crystals are plotted in Figures 3d and e, while Figures 3f and g display n and k, respectively, for both the cleaved and thin film uniaxial models. Here we retain high sensitivity to the transparent region birefringence due to back reflections through the ~2 micron thick crystals (visible as the asymmetric tilt of oscillations in Fig. 3d and e). However, we are less sensitive to the extraordinary absorption without the tSE data. Therefore, we fix the critical points in the extraordinary axis dielectric function to those deduced for the thin film. The anisotropic model deduced for PEPI thin films fits the ellipsometric data for the cleaved crystals over a broad range of frequency (Fig. 3d,e) and the extracted optical constants for both samples show similar energy-dependent anisotropy (Fig. 3f,g). We also confirmed the orientation of these crystals with a full Mueller Matrix analysis. We find that the cross-polarization components are negligible, and therefore the crystal can be accurately and completely described as a uniaxial medium oriented with the optical c-axis perpendicular to the surface we are measuring, as expected for PEPI's natural cleavage direction.

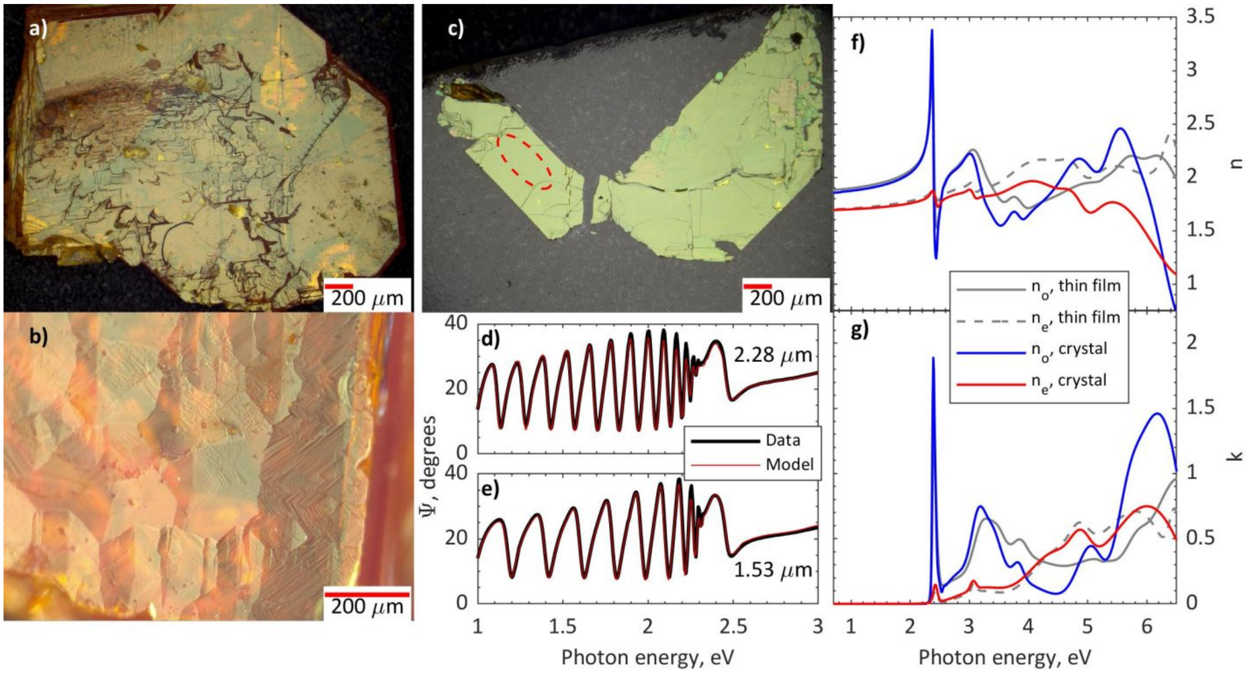

Figure 3: Bulk and cleaved crystal analysis. (a), (b) Optical micrographs of as-grown bulk crystals exhibiting surface defects, step edges, and tilted facets which confound ellipsometric analysis. Cleaved crystals (c) yield smooth, uniform domains on the scale of our measurement volume (red dashed ellipse). Ellipsometry from such cleaved crystals around 2μm or thinner (d), (e) is well fit by slightly relaxed models developed for the thin films. (f), (g) Modeled optical constants for these cleaved crystals (red and blue) and the thin film (grey).

Density Functional Theory Calculations

To better understand the electronic origins and spectral dependence of the observed optical anisotropy, we turn to DFT calculations. For the atomic structure underlying the simulations, semilocal DFT including van-der-Waals correction (here, Perdew-Burke-Ernzerhof (PBE) functional [36] with Tkatchenko-Scheffler (TS) pairwise dispersion scheme correction [37]) is known to provide reliable results for hybrid organic-inorganic perovskites [38]. Since alignment of electronic levels between the components may be important, a high-level (and, for the 188-atom unit cell of PEPI, computationally demanding) approach beyond semilocal DFT is employed for the electronic structure and dielectric properties (here, the Heyd-Scuseria-Ernzerhof (HSE06) hybrid density functional [28,39,40]). We rely on the HSE06 parameters suggested by Krukau *et al.* [40], i.e., α=0.25 for the exchange mixing parameter and ω=0.11 (atomic units)$^{-1}$, since this choice has yielded correct energy level alignments between organic and inorganic components in our own past work [26,38] and does not introduce a material-specific fitting of key parameters of the hybrid density functional (see SI section S2.1 of the SI for further discussion). For investigation of the optical properties of PEPI from first principles, it is essential to treat spin-orbit coupling (SOC) effects, here included in a second-variational approach [31], recently benchmarked for hybrid perovskites in Ref. [41]. The electronic levels arising from Pb (and also to a lesser extent those of lighter I) split substantially due to SOC, which leads to pronounced changes in the arrangement of electronic bands in the conduction band [38,42,43]. Leveillee et al. performed an in-depth study of the imaginary part of the dielectric function of PEPI and provided an analysis of the electronic transitions that give rise to the absorption spectrum [44]. However, to our knowledge, the dependence of the dielectric function on different crystal directions has not yet been investigated for PEPI.

Figure 4a shows the unit cell of PEPI after relaxation of the experimentally determined atomic positions [45] with DFT-PBE+TS. As shown in Table S1, the computational lattice parameters are within 1% of low-temperature experimental lattice parameters (note that zero-point vibrations and thermal expansion are not accounted for in the DFT calculations). As in Figure 1a, the inorganic and organic layers are stacked in ***a***-direction. Electronic structure calculations with DFT-HSE06+SOC reveal a direct band gap of 2.01 eV, which is smaller than the experimentally expected fundamental band gap of ~2.5-2.8 eV [19,46–51] . A band gap of 1.95 eV, similar to our DFT-HSE06+SOC gap, was predicted by Leveillee et al. for PEPI with HSE06+SOC within VASP [44]. The slight difference in band gap between our calculations and Leveillee *et al.*'s study can likely be attributed to the different treatment of SOC in VASP (code used by Leveille *et al.*) and FHI-aims (code used in this work).

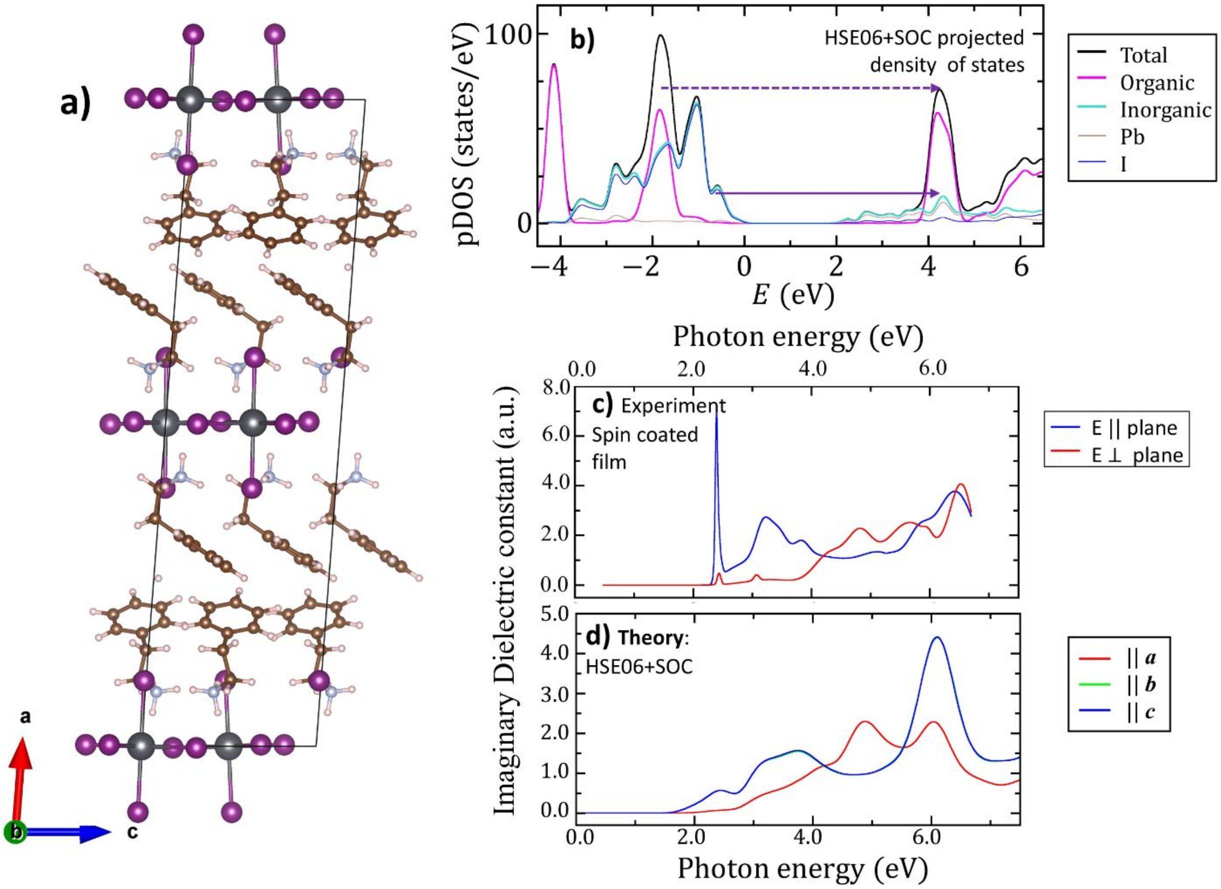

Figure 4: a) Unit cell of PEPI used in the computations. b) DFT-HSE06+SOC density of states projected onto all atoms (black, total), the organic molecules (thick magenta), the inorganic framework (thick green), the Pb atoms (grey) and the I atoms (dark blue). The dashed and solid purple arrows indicate two possible transitions. c) Experimental measurement of the imaginary dielectric constant from the spin coated film. d) Imaginary dielectric constant as a function of energy between 0 and 7.5 eV along ***a** (red)*, ***b*** (green) and ***c*** direction (blue). Note that the line from ***b*** disappears almost entirely under the one from ***c***; the dielectric constant within the plane of the inorganic layers (i.e. in ***b*** and ***c***-direction) is equivalent.

The underestimation of the computed band gap (2.01 eV), relative to the experimentally reported range for the fundamental gap, is an expected systematic error of the HSE06+SOC method as used here (see SI, section S2 for more details) [26,31]. Importantly, the DFT methods applied here are restricted to single-particle band-to-band transitions and cannot account for excitonic effects in the dielectric properties, whereas experimentally determined optical data are dominated by the excitonic transition. However, numerically converged many-body treatments capable of capturing excitonic excitations from first principles remain as yet out of reach for complex materials with the unit cell size considered here [52]. Excitonic effects will instead be covered semi-empirically by k.p calculations further below.

In Figure 4b, we plot the density of states projected onto the organic and inorganic components and show that PEPI exhibits a type-I level alignment where the frontier orbitals are on the inorganic framework, as expected from the small aromatic system of the organic cation and as also observed previously [44]. The valence band maximum is mainly formed by I-contributions while the conduction band minimum is due to mostly Pb and I contributions, in agreement with previous observations [53] (see also Figure S4 for the band structure). The predicted bandgap of the organic carbon framework is 4.8 eV, close to the 4.6 eV gap observed experimentally for the $S_0 \rightarrow S_1$ (π-π^*) transition in solid benzene [54].

Figure 4d shows the HSE06+SOC-derived frequency-dependent *single-particle* imaginary dielectric constant as a function of the photon energy, using the computational approximations described in Ref. [55] and decomposed into the in-plane (ordinary, parallel to ***b*** and ***c*** crystal axis) and out-of-plane contribution (extraordinary, dielectric function along ***a***). A detailed decomposition of the computational transitions that contribute to the dielectric function, shown in Figure S5, demonstrates that, for both ordinary and extraordinary axes, contributions to the absorption spectrum below 3.5 eV can be attributed to transitions purely within the inorganic framework. Transitions purely within the organic framework start well above 5 eV in the computed dielectric function.

In comparison to the experimental data in Figure 4(c), the qualitative trends predicted for the ordinary and extraordinary spectra are reproduced in the calculated spectra, although with somewhat different shifts of inorganic- and organic-derived features. The experimental peaks between 3.25 eV – 4 eV in the imaginary ordinary dielectric function are reflected in the calculated spectrum and are attributed to within-inorganic transitions, as described above. Likewise, the rise of the extraordinary, imaginary dielectric function in the experiment at ~3.8 eV is reproduced qualitatively and can be attributed to a higher DOS in the inorganic, allowing stronger single-particle transitions. Based on the observations discussed in the previous paragraph and the separation between the two strong organic contributions in the projected DOS of ~6.5 eV (Fig. 4b, dashed purple line), we attribute the peak around ~6.5 eV to predominantly organic-organic π-π^* transitions (see also discussion on hybridized orbitals below). Quantitative deviations between theory and experiment in the detailed structure of the imaginary dielectric function and computed absorption coefficient must be expected and are due to the remaining approximations made in hybrid DFT as well as due to the neglect of excitonic effects in the calculations. For example, the absence of a sharp peak at the fundamental gap in the calculated *single-particle* imaginary dielectric constant in Figure 4(d) provides unambiguous evidence for the excitonic nature of the peak at 2.4 eV in the experimental data plotted in Figure 4(c). Otherwise, the qualitative match is clear.

k · p Calculations

Having theoretically considered the contribution of single-particle optical transitions to the experimentally observed optical anisotropy, we now focus on the near band edge dielectric response and then consider excitonic transitions (see also SI section S3 and S4 for additional details). In the absence of excitonic effects, the imaginary part of the dielectric function associated with polarization along direction $\hat{u}$, which we denote as $Im\,\epsilon_{uu}(\omega)$, is determined by the sum, [56]

$$Im\,\epsilon_{uu}(\omega) = \frac{4\,\pi^2 e^2}{m_0^2\,\omega^2}\sum_{c,v}\frac{1}{V}\sum_{\boldsymbol{k}}|\hat{u}\cdot\,\boldsymbol{p}_{c,v}(\boldsymbol{k})|^2\,\delta(E_c(\boldsymbol{k}) - E_v(\boldsymbol{k}) - \hbar\omega). \tag{1}$$

In Eq. 1, m_0 and e denote the free electron mass and charge, respectively, and $\boldsymbol{p}_{c,v}(\boldsymbol{k})$ is the interband momentum matrix element between conduction band (CB) state $c,\boldsymbol{k}$ and valence band (VB) state $v,\boldsymbol{k}$. Near the band edge, the Bloch functions $u_{n,\boldsymbol{k}}$ for a given band, n, can be approximated by the band edge functions u_{n0}. Using this approximation and recasting Eq.1 in terms of the total oscillator strength f_u for polarization $\hat{u}$, for a given $\boldsymbol{k}$, the imaginary part of the dielectric function can be approximated for energies near the band gap by (derivation in the SI),

$$Im\,\epsilon_{uu}(\omega) \approx \frac{2\hbar\,\pi^2 e^2}{m_0\,\omega}\,f_u\,\,\frac{1}{V}\sum_{\boldsymbol{k}}\delta(E_c(\boldsymbol{k}) - E_v(\boldsymbol{k}) - \hbar\omega)\,. \tag{2}$$

The polarization dependence of the oscillator strength depends on the valence and conduction band edge Bloch functions at $\boldsymbol{k} = 0$. For MHPs, the VB Bloch functions can be represented in K.P theory as the 2-fold degenerate states with total angular momentum $J = 1/2,\ J_z = \pm\,1/2$ with S orbital symmetry: [57,58]

$$u^v_{\frac{1}{2},\frac{1}{2}} = S\uparrow, \qquad u^v_{\frac{1}{2},-\frac{1}{2}} = S\downarrow. \tag{3}$$

Here, the symbol S denotes an orbital function that transforms as an invariant under the operations of the crystal point symmetry group, while ↑ (↓) denote the spin functions with projection $S_z = +1/2\ (-1/2)$. The isotropic in-plane response in Fig 4(c,d) suggests a quasi-tetragonal model for the CB Bloch functions in which they are represented as functions with total angular momentum projection $J_z = \pm\frac{1}{2}$: [32,58–60]

$$u^c_{\frac{1}{2}} = -\left\{\sin\theta Z\uparrow + \cos\theta\frac{(X+i\,Y)}{\sqrt{2}}\downarrow\right\};\qquad u^c_{-\frac{1}{2}} = \left\{-\cos\theta\frac{(X-i\,Y)}{\sqrt{2}}\uparrow + \sin\theta\, Z\downarrow\right\}. \tag{4}$$

Here, the phase angle θ reflects the mixing of $P_{1/2}$and $P_{3/2}$ states due to the anisotropic confinement of associated with the inorganic layers, which has been previously described in the literature in terms of a phenomenological effective tetragonal crystal field. The value of θ is determined by the SOC split-off parameter Δ_{SO} and the effective crystal field δ by [32,59,60]

$$\tan 2\theta = \frac{2\sqrt{2}\,\Delta_{SO}}{\Delta_{SO} - 3\delta}, \qquad \theta \leq \frac{\pi}{2}. \tag{5}$$

Using Eq 3-4 we find that the oscillator strength associated with the two in-plane directions (x, y) are equal $(f_x = f_y = f_{\parallel})$, as expected based on the in-plane isotropy observed in the hybrid DFT calculation in Fig. 4. The ratio of the out-of-plane oscillator strength $f_\perp$ to the in-plane oscillator strength $f_\parallel$ and the corresponding ratios of the dielectric response are determined by the phase angle θ:

$$\frac{f_\perp}{f_\parallel} = 2\tan^2\theta = \frac{Im\,\epsilon_{aa}(\omega)}{Im\,\epsilon_{bb}(\omega)} = \frac{Im\,\epsilon_{aa}(\omega)}{Im\,\epsilon_{cc}(\omega)} \tag{6}$$

This identification allows us to determine the band edge oscillator strength ratio $f_\perp/f_\parallel$ directly from the DFT calculations such as shown in Fig. 4d. In Figure S7 we plot the ratio $Im\,\epsilon_{zz}(\omega)/Im\,\epsilon_{xx}(\omega)$ calculated as in Fig 4, but using semilocal DFT-PBE+SOC, which allows us to use a tighter *k*-space grid (3x15x15). A Gaussian broadening function is applied, with full-width at half-maximum (FWHM) set to 100 meV. The ratio at the band edge is 7.7% and increases with increasing energy. At an energy 120 meV above the band edge, (a correction corresponding to the kinetic energy of the 1S exciton state, see SI section S5.2), the ratio increases to 8.7%. In the SI Section S4, we use the multiband effective mass theory to show that the ratio of the oscillator strength of the lowest energy *exciton* transition for polarization perpendicular versus parallel to the lead-halide sheets, $f_{\perp}{}^{exc}/f_{\parallel}{}^{exc}$, is also given by Eq. 6. Using Eq. 6, this implies $\sin\theta = 0.193$ at the band edge and an average value $\sin\theta = 0.204$ for the 1S exciton. For reference, the tetragonal crystal field parameter in a similar PbI_4-based 2D MHP has been previously reported as $\sin\theta = 0.227$ [59] while for $PbBr_4$-based 2D MHPs the measured range is $\sin\theta = 0.2 - 0.32$ [60,61].

Consequently, based on the DFT calculations, we expect $f_{\perp}{}^{exc}/f_{\parallel}{}^{exc}$=8.7% for PEPI. This value is somewhat higher than the experimentally determined ratios shown in Table 1 of 5.9% and 6.5% for cleaved crystal and thin film samples, respectively. One element missing from this analysis is the fact that the excitons are embedded in a *dielectric superlattice*. That is, excitons are confined to the 2D lead-halide layers with a relatively high background dielectric constant which is surrounded by organic layers with a lower dielectric. The resulting anisotropic dielectric environment causes a significant enhancement of the anisotropy of the optical response above what would be expected solely due to the intrinsic exciton anisotropy as explored in recent studies by Smith et. al. [62] and by DeCresent et al. [24]. In SI section S5.1 of the SI we apply the effective medium model of DeCresent to back-calculate the intrinsic anisotropy from the experimentally measured anisotropy, accounting for the dielectric anisotropy effect under the assumption that the interfaces between the 2D lead-halide layers and the organic layers may be considered classically as abrupt dielectric interfaces. Using the experimental value $\left(f_{\perp}{}^{exc}/f_{\parallel}{}^{exc}\right)_{meas} = 5.9\% \pm 1\%$ this results in a corrected estimate of the intrinsic anisotropy of $\left(f_{\perp}{}^{exc}/f_{\parallel}{}^{exc}\right)_{intr} = 16.6 \pm 3\%$, as compared to the estimate based on DFT+PBE+SOC of 8.7%. This discrepancy, about 48% for the cleaved crystal sample, may be due the fact that the DFT methods applied here are restricted to single-particle band-to-band transitions and do not account for excitonic effects, which are modelled within a simple effective mass approximation, or alternately due to a failure of the classical dielectric interface model employed to estimate the local field screening corrections, which assumes abrupt dielectric interfaces. As an independent check of the reasonableness of the effective mass model and the intrinsic dielectric parameters recovered using the dielectric anisotropy model of DeCresent, we made a calculation of the exciton binding energy using the dielectric parameters tabulated in Table S4 which were extracted from analysis of the ellipsometry data at the exciton line (see SI section S5.2). This calculation accounts for the electron-hole image charge interactions in the dielectric superlattice using the exact expressions of Guseinov [63], and employs the experimental reduced effective mass of 0.087 Dyksik et al. [64], which is in reasonable agreement with the value calculated using hybrid DFT (0.110, see SI section S2.2). The calculated 1s exciton binding energy is 259 meV, in excellent agreement with the value of 250 meV originally reported by Kitazawa [46] and the value of 265 meV recently reported by Dyksik et al. [64] This value of exciton binding energy would suggest a fundamental (electronic) bandgap of ca. 2.65 - 2.68 eV for PEPI, based on the observed optical bandgap (i.e. peak of the lowest energy fitted exciton state) of ca. 2.39 – 2.42 eV (Table 1).

Another check of our results is afforded by application of the effective mass theory to make an estimate of the effective crystal field, δ, by accounting for quantum-confinement-induced mixing between the $P_{1/2}$ and $P_{3/2}$ conduction band states. The approach, described in Section S6 of the ESI, utilizes a quantum well model for the inorganic layer [38] based on the Luttinger Hamiltonian modified for the "inverted" band ordering of the perovskites [65], which leads to mixing of the frontier conduction bands with the upper "light electron" conduction band. The analysis results in an expression relating the effective crystal field to the bandgap energy, E_g, the Kane energy, E_p, and the inorganic layer thickness: [66]

$$\delta = -\frac{\hbar^2}{2m_0}\frac{E_p}{E_g}\left(\frac{\pi}{d}\right)^2 . \tag{7}$$

The Kane energy in turn can be found from the exciton oscillator strength per unit area measured here for polarization parallel to the inorganic layers, which is unaffected by the dielectric discontinuity discussed above, using the relation [67],

$$E_p = \hbar\omega \frac{f_{\parallel}^{exc}\pi a_{10}^2}{S}\,\frac{1}{8\,cos^2\theta}. \tag{8}$$

Here, $\hbar\omega$ is the exciton transition energy, $f_{\parallel}^{exc}/S$ is the oscillator strength per unit area for polarization parallel to the inorganic layers, a_{10} is the calculated 2D exciton radius (see ESI Table S5), and phase angle

θ is determined as $sin\theta = 0.277$ using the intrinsic oscillator strength ratio $\left(f_{\perp}{}^{exc}/f_{\parallel}{}^{exc}\right)_{intr}$=0.166 determined from the measured oscillator strength ratio using Eq. S67. Using the parameters in Table 1 and Table S6 corresponding to the cleaved crystal sample, we find the Kane energy $E_p = 3.98$ eV and the effective crystal field $\delta = -1.36$ eV; these values are close to the respective values $E_p = 5.5$ eV and $\delta = -1$eV calculated for 4F-PEPI ($[pFC_6H_5C_2H_4NH_3]_2PbI_4$) using DFT in Ref. [57]. The analysis here in terms of the quantum well model then enables determination of the SOC split-off parameter using Eq. 5, yielding $\Delta_{SO} = 1.2$eV, which matches both the value calculated from the splitting of the $P_{1/2}$ and $P_{3/2}$ conduction band states at the Γ point in DFT-HSE+SOC (See ESI Sec. 6) as well as the value determined via DFT for 4F-PEPI in Ref. [57].

Our DFT calculations in conjunction with k · p and effective mass calculations for the exciton, in agreement with other recent studies [22], demonstrate that the PEPI exciton dipole matrix is not strictly zero in the out-of-plane polarization. The ellipsometry results on PEPI thin films and crystals allow us to extract the oscillator strength for the sharp 2.4 eV exciton resonance in both the ordinary and extraordinary axes. We find less than 10% deviation for the oscillator strengths extracted from either thin film or crystals for a particular axis. We also see a 20% sharpening of the excitonic modes of crystals, as modeled in the ordinary axis critical points, likely reflecting the effects of inhomogeneous broadening of the excitonic transition in thin films.

	Axis	Oscillator strength, f ($^{1}/_{cm^2}$)	Linewidth, ε_2 (meV)	Energy	$f_{\perp}{}^{exc}/f_{\parallel}{}^{exc}$
Thin film, isotropic model		$3.9 \times 10^{13} \pm 8 \times 10^{12}$	60	$2.395\ eV \pm$	
Thin film, uniaxial model	IP	$3.4 \times 10^{13} \pm 3 \times 10^{11}$	57	$2.394\ eV \pm$	6.5% ± 2%
	OP	$2.2 \times 10^{12} \pm 1 \times 10^{12}$	86	$2.419\ eV \pm$	
Cleaved crystal, uniaxial model	IP	$3.6 \times 10^{13} \pm 8 \times 10^{12}$	44	2.385 ± 5 n	5.9% ± 1%
	OP	$2.2 \times 10^{12} \pm 1 \times 10^{12}$	86	$2.419\ eV \pm$	

Table 1: Exciton linewidth and oscillator strength determined from critical points in PEPI thin film and cleaved crystals. Oscillator strength is calculated as a sum of multiple terms in the exciton structure, and energy is reported as the dominant, lowest energy point. Note that the OP critical points for the cleaved crystal are fixed to the results from the thin film. See the Experimental Methods for details. Confidence intervals reported correspond (+/-) fit error magnitudes estimated in CompleteEASE, i.e. estimating error on the model.

Discussion and Outlook

Here, we have determined the uniaxial optical constants of spin-coated thin films of a prototypical 2D lead-halide perovskite PEPI. The significant optical anisotropy of PEPI means that any isotropic model will produce unphysical results, and our optical constants model can serve as an effective starting point for characterizing film quality and nonidealities, calibrating quantum yield, or designing optoelectronic devices. Furthermore, we show that the optical constants, qualitative frequency-dependent anisotropy, birefringence in the transparency region, and exciton oscillator strengths for PEPI thin films are in excellent agreement with findings for cleaved crystals. This indicates that the PEPI thin films form with the PbI4 quantum wells highly aligned in-plane. One might hypothesize that this is seeded due to either the organic or the inorganic preferentially bonding to the substrate surface, or due to the dynamics of the drying seeding order at the solvent-air interface. Either way, we do not require perfect *in-plane* order to have reasonably good agreement between n,k of the film to the crystal—both DFT and ellipsometry suggest that the crystal can be described by a uniaxial description. It just so happens that the solution processed film does align such that the extraordinary axis is normal to the substrate. An important clarification is that a noticeable sharpening of the critical points occurs in the crystal, which could imply a general (and expected) improvement in crystal quality.

The good qualitative match between our experimentally observed optical anisotropy and that predicted for single-particle and excitonic transitions in an idealized 2D PEPI structure suggests a high degree of in-plane alignment of the 2D lead-halide sheets in both spin-coated thin films and cleaved crystals. While prior studies on spin-coated PEPI films suggest a high degree of in-plane alignment, the precise degree of alignment is rarely quantified. Importantly, the ratio of extraordinary/ordinary oscillator strengths for the excitonic transition that we extract *via* ellipsometry for PEPI thin films is quite close to the ratio predicted by DFT calculations (as noted above, using DFT-PBE+SOC for the calculation of the ratio, in order to achieve dense k-space integration) in conjunction with a multi-band effective mass model of the excitonic response for a perfectly ordered PEPI crystal ${}^{f_z}\!/_{f_x} \approx 8.7\%$. Using the values in Table 1, we arrive at ratios of $({}^{f_z}\!/_{f_x} \approx 6.5\%)$ for PEPI thin films and $({}^{f_z}\!/_{f_x} = 5.9\%)$ for cleaved crystals without correction for local field screening effects; accounting for these corrections within a classical dielectric interface model we find ${}^{f_z}\!/_{f_x} \approx 18.3\%$ and ${}^{f_z}\!/_{f_x} = 16.6\%$ for the thin film and cleaved crystal samples, respectively. The correspondence between the measured and the theoretical anisotropy suggests that, to within the accuracy of our ellipsometry and computational analyses, we cannot detect statistically significant out-of-plane disorder in our spin-coated or cleaved PEPI crystals. This apparent high degree of alignment is an especially intriguing result for a spin-coated thin film where the formation of the perovskite layers happens dynamically and rapidly.

Our results also emphasize the strong connection between structural anisotropy in 2D perovskites and the contribution of specific organic and inorganic orbitals to optical transitions polarized along a particular axis. Our discussion of the hybrid DFT calculations above focuses on organic-to-organic and inorganic-to-inorganic optical transitions. However, Leveillee *et al.* [44] recently suggested that transitions including both the organic and inorganic component contribute to peaks in the region above 3.8 eV, based on DFT-PBE+SOC calculations, where the CBM was shifted to match the position of the HSE06+SOC CBM. To investigate this observation, in Figure S5, we show a decomposition of the imaginary dielectric constant according to the character of the transition. In agreement with Leveillee *et al.*, we find that the dielectric constant above 3.8 eV involves numerous transitions between orbitals to which both organic and inorganic components contribute. As shown in Figure S6 for one exemplary eigenstate in the valence band, the electronic density in these orbitals is likely hybridized between organic and inorganic components.

We note that while a transition may take place between hybridized orbitals, the dipole operator used to express the dielectric response in the HSE06+SOC calculations within the random-phase approximation [68] and the implementation of Ref. [55] is a local operator. This means that a transition can (computationally) only happen at the same spatial point, i.e., the generalized Kohn-Sham orbitals between the organic and inorganic components or vice versa must overlap if a transition is labeled as occurring between the components. The peak of the dielectric constant around ~6.5 eV is indeed due to mostly within-organic transitions, since a decomposition of the dielectric constant in Figure S5 in the supplementary material shows that organic to hybrid orbitals contribute mainly to this feature.

Our investigation also illustrates that while much additional information can be derived from theoretical analysis of the spectra, such an analysis is very far from straightforward. Methodological development towards understanding the optoelectronic spectra of hybrid organic-inorganic perovskites is hence severely needed, and first attempts are already on the way [69].

Conclusion

In this study, we demonstrate that optical anisotropy must be considered to accurately understand and quantify optical processes in 2D MHPs semiconductors. As solution-processed, partially transparent semiconductors, perovskites are highly amenable to multimodal ellipsometric analysis. Interestingly, we find that spin-coated thin films of PEPI exhibit a high degree of order, with anisotropic optical constants very similar to that of an exfoliated single crystal. Combining this detailed spectroscopic study with high-level DFT and $k \cdot p$ theory allows us to estimate, in a self-consistent manner, the in-plane and out-of-plane optical constants, exciton binding energy, and fundamental electronic bandgap of the prototypical 2D perovskite PEPI. These results highlight the potential roles that perovskite dimensionality, chemical composition, and organic/inorganic coupling may play in tuning the energy, polarization, and oscillator strength of optical transitions. Such tunability is attractive for optoelectronic technologies such as solar cells, light-emitting diodes, and lasers. Importantly, the combination of multimodal ellipsometry and structural tools (e.g. XRD) with high-fidelity computations is shown to be particularly valuable for providing deeper understanding of the fundamental optical transitions in low-dimensional perovskites. As such, our study provides a framework for accurately extracting the optical constants of these anisotropic semiconductors, a prerequisite for rational design and optimization of these envisioned applications.

Author contributions

M.S. S.M.J and P.C.S wrote the manuscript with contributions from all authors. M.S. conceived of and coordinated the collaboration and conducted the ellipsometry analysis. P.C.S. conducted the K.P and effective mass calculations. S.M.J., X.Q., V.W.Y, and V.B. conducted the DFT analysis. B.W.L., H.L., and J.L.B. synthesized and prepared thin films and exfoliated crystals.

Acknowledgements

This work was authored in part by the National Renewable Energy Laboratory (NREL), operated by Alliance for Sustainable Energy, LLC, for the U.S. Department of Energy (DOE) under Contract No. DE-AC36-08GO28308. This work was primarily supported by the Center for Hybrid Organic Inorganic Semiconductors for Energy (CHOISE) an Energy Frontier Research Center funded by the Office of Science, Office of Basic Energy Sciences within the U.S. DOE. M.S. gratefully acknowledges funding from NREL's LDRD fund for development of ellipsometric methodology. S.M.J gratefully acknowledges a WIRL-COFUND fellowship at the University of Warwick, under the Marie Skłodowska Curie Actions COFUND program (grant agreement number 713548) for support during analysis of computational data and while contributing to the manuscript text. V. W.-z. Yu was supported by a fellowship from the Molecular Sciences Software Institute under National Science Foundation (NSF) Award No. 1547580 for development of DFT-related, computational software infrastructure. This research used resources of the National Energy Research Scientific Computing Center (NERSC), a U.S. DOE Office of Science User Facility operated under Contract No. DE-AC02-05CH11231. Additionally, this work used resources of the Extreme Science and Engineering Discovery Environment (XSEDE), which is supported by NSF grant number ACI-1548562. This work used the XSEDE resource Stampede2 at the Texas Advanced Computing Center through allocation TG-DMR200077. An award of computer time was provided by the INCITE program. This research used resources of the Argonne Leadership Computing Facility, which is a DOE Office of Science User Facility supported under Contract DE-AC02-06CH11357. The views expressed in the article do not necessarily represent the views of the DOE or the U.S. Government. The U.S. Government retains and the publisher, by accepting the article for publication, acknowledges that the U.S. Government retains a nonexclusive, paid-up, irrevocable, worldwide license to publish or reproduce the published form of this work, or allow others to do so, for U.S. Government purposes. The authors would also like to acknowledge valuable input from James Hilficker at J. A. Woollam in regard to fitting and interpreting ellipsometry results.

Methods

All first-principles density functional theory (DFT) calculations were performed within the all-electron electronic structure code FHI-aims [29,30,70–72]. We first optimized the geometry of PEPI based on an X-ray structure using DFT-PBE+TS, a (2×8×8) k-space grid and FHI-aims' "tight" numerical settings. We used the X-ray structure of Du et al., space group number 2, $P\overline{1}$, as an initial structure for our relaxation [45]. No space group symmetry was enforced during the relaxation. Based on the DFT-PBE+TS relaxed geometries, we performed electronic structure calculations with the hybrid exchange-correlation HSE06 functional with $\alpha = 25~\%$ Hartree Fock exchange and a screening parameter of 0.11 (Bohr radii)$^{-1}$ [28,39,40]. We account for spin-orbit-coupling (SOC) effects at the level of 2nd variational non-self-consistent SOC [31]. Using DFT-HSE06+SOC, the imaginary dielectric constant as a function of energy was calculated within the independent particle approximation based on the imaginary and real dielectric function [68,73–75] using the method of Ref. [55] with a Gaussian broadening width of 0.2 eV on a $(3 \times 7 \times 7)$ k-grid.

Atomic structures were plotted using VESTA [76].

Sample Preparation

An 80 nm thick film of PEPI was prepared on a fused silica substrate. The powders phenethylammonium iodide (PEAI) and PbI_2 (Aldrich) were weighed out in the glovebox and dry DMF was added to prepare a 0.2 M solution based on Pb. In air, the 80 nm thick PEPI film was prepared by dropping 120 µL of solution onto a quartz substrate, followed by spinning at 4,000 rpm for 60 seconds. After spinning, the sample was transferred to a preheated hotplate (120 °C) and annealed for 10 minutes.

2D perovskite PEPI single crystals are synthesized based on previously reported slow-cooling method [77]. Briefly, 200 mg (0.90 mmol) of PbO and 200 µL (1.59 mmol) of phenylethylammonium are fully dissolved in 4 mL of HI and 0.5 mL of H_3PO_2 solution at 90 °C. The solution is then slowly cooled to room temperature at a rate of 2 °C/h, giving orange sheet-like crystals. The crystals are then isolated from the parent solution by vacuum filtration, washed by a small amount of diethyl ether, and dried under vacuum. Thin crystals were exfoliated from the parent crystal using stiff heat release tape that serves as a handle. Sequential exfoliation steps with the tape yield successively thinner crystals. Many crystals were surveyed to select the best surface quality, flatness, and area. Below ~1 µm thickness the crystals tended to fracture into areas too small to measure.

Optical methods:

Transmittance was collected on a Cary 7000 UV-VIS-NIR spectrophotometer for maximum precision in the OD measurement. rSE was collected on a JA Woollam M2000DI at 45° to 75° using tape to suppress backside reflections, and tSE was collected on a JA Woollam M2000DI from -10° to 70°. The three data sets were processed as a multisample analysis in CompleteEASE. For bulk and cleaved crystals, rSE and reflection Mueller Matrix were collected using focus probes and either a JA Woollam M2000 or RC2, respectively.

For thin films, a single layer on the fused silica substrate was used for the model. Surface roughness (50% Bruggeman effective medium approximation (EMA)) was included to significantly improved the (RMSE). Cleaved crystals are modeled as a uniform film on a Cauchy substrate (an approximation of the heat release tape) with up to two EMA roughness layers.

Initial fitting:

To investigate the validity of the anisotropic model, we first apply a BSpline optical constant model [78]. The substrate was previously characterized, including quantifying UV absorption. To extend the interpretation of these results, we replace the BSplines with general oscillators [79]. This allows us to identify critical points, further constrains the model, and increases speed of fitting with only minimally increasing the RMSE. All oscillators are modeled as Gaussians except for one PSemiM0 at approximately 2.546 eV. We additionally test for grading of the layer and thickness nonuniformity, but these do not improve the fit, so we disregard them.

References

[1] K. Wang, D. Yang, C. Wu, M. Sanghadasa, and S. Priya, *Recent progress in fundamental understanding of halide perovskite semiconductors,* Prog. Mater. Sci. **106**, 100580 (2019) http://doi.org/10.1016/j.pmatsci.2019.100580.

[2] A. Kojima, K. Teshima, Y. Shirai, and T. Miyasaka, *Organometal halide perovskites as visible-light sensitizers for photovoltaic cells,* J. Am. Chem. Soc. **131**, 6050 (2009) http://doi.org/10.1021/ja809598r.

[3] H. S. Kim, C. R. Lee, J. H. Im, K. B. Lee, T. Moehl, A. Marchioro, S. J. Moon, R. Humphry-Baker, J. H. Yum, J. E. Moser, M. Grätzel, and N. G. Park, *Lead iodide perovskite sensitized all-solid-state submicron thin film mesoscopic solar cell with efficiency exceeding 9%,* Sci. Rep. **2**, 1 (2012) http://doi.org/10.1038/srep00591.

[4] Y. H. Kim, H. Cho, and T. W. Lee, *Metal halide perovskite light emitters,* Proc. Natl. Acad. Sci. U. S. A. **113**, 11694 (2016) http://doi.org/10.1073/pnas.1607471113.

[5] N. Wang, L. Cheng, R. Ge, S. Zhang, Y. Miao, W. Zou, C. Yi, Y. Sun, Y. Cao, R. Yang, Y. Wei, Q. Guo, Y. Ke, M. Yu, Y. Jin, Y. Liu, Q. Ding, D. Di, L. Yang, G. Xing, H. Tian, C. Jin, F. Gao, R. H. Friend, J. Wang, and W. Huang, *Perovskite light-emitting diodes based on solution-processed self-organized multiple quantum wells,* Nat. Photonics **10**, 699 (2016) http://doi.org/10.1038/nphoton.2016.185.

[6] X. Zhu, Y. Lin, J. San Martin, Y. Sun, D. Zhu, and Y. Yan, *Lead halide perovskites for photocatalytic organic synthesis,* Nat. Commun. **10**, 1 (2019) http://doi.org/10.1038/s41467-019-10634-x.

[7] S. Hong, S. H. Choi, J. Park, H. Yoo, J. Y. Oh, E. Hwang, D. H. Yoon, and S. Kim, *Sensory Adaptation and Neuromorphic Phototransistors Based on CsPb(Br1- xIx)3Perovskite and MoS2Hybrid Structure,* ACS Nano **14**, 9796 (2020) http://doi.org/10.1021/acsnano.0c01689.

[8] Y. Fu, H. Zhu, J. Chen, M. P. Hautzinger, X. Y. Zhu, and S. Jin, *Metal halide perovskite nanostructures for optoelectronic applications and the study of physical properties,* Nat. Rev. Mater. **4**, 169 (2019) http://doi.org/10.1038/s41578-019-0080-9.

[9] F. Zhang, H. Lu, J. Tong, J. J. Berry, M. C. Beard, and K. Zhu, *Advances in two-dimensional organic-inorganic hybrid perovskites,* Energy Environ. Sci. **13**, 1154 (2020) http://doi.org/10.1039/c9ee03757h.

[10] G. Grancini, C. Roldán-Carmona, I. Zimmermann, E. Mosconi, X. Lee, D. Martineau, S. Narbey, F. Oswald, F. De Angelis, M. Graetzel, and M. K. Nazeeruddin, *One-Year stable perovskite solar cells by 2D/3D interface engineering,* Nat. Commun. **8**, 1 (2017) http://doi.org/10.1038/ncomms15684.

[11] Z. Wang, Q. Lin, F. P. Chmiel, N. Sakai, L. M. Herz, and H. J. Snaith, *Efficient ambient-air-stable solar cells with 2D-3D heterostructured butylammonium-caesium-formamidinium lead halide perovskites,* Nat. Energy **2**, 1 (2017) http://doi.org/10.1038/nenergy.2017.135.

[12] T. Zhang, M. Long, M. Qin, X. Lu, S. Chen, F. Xie, L. Gong, J. Chen, M. Chu, Q. Miao, Z. Chen, W. Xu, P. Liu, W. Xie, and J. bin Xu, *Stable and Efficient 3D-2D Perovskite-Perovskite Planar Heterojunction Solar Cell without Organic Hole Transport Layer,* Joule **2**, 2706 (2018) http://doi.org/10.1016/j.joule.2018.09.022.

[13] W. Huang, T. Bu, F. Huang, and Y. B. Cheng, *Stabilizing High Efficiency Perovskite Solar Cells with 3D-2D Heterostructures,* Joule **4**, 975 (2020) http://doi.org/10.1016/j.joule.2020.04.009.

[14] Y. H. Kim, H. J. Kim, M. Osada, B. W. Li, Y. Ebina, and T. Sasaki, *2D perovskite nanosheets with thermally-stable high-κ response: A new platform for high-temperature capacitors,* ACS Appl. Mater. Interfaces **6**, 19510 (2014) http://doi.org/10.1021/am506629g.

[15] X. Hong, T. Ishihara, and A. V. Nurmikko, *Photoconductivity and electroluminescence in lead iodide based natural quantum well structures,* Solid State Commun. **84**, 657 (1992) http://doi.org/10.1016/0038-1098(92)90210-Z.

[16] M. D. Smith, B. A. Connor, and H. I. Karunadasa, *Tuning the Luminescence of Layered Halide Perovskites,* Chem. Rev. **119**, 3104 (2019) http://doi.org/10.1021/acs.chemrev.8b00477.

[17] S. L. Guillot, K. S. Mistry, A. D. Avery, J. Richard, A.-M. Dowgiallo, P. F. Ndione, J. van de Lagemaat,

M. O. Reese, and J. L. Blackburn, *Precision printing and optical modeling of ultrathin SWCNT/C $_{60}$ heterojunction solar cells,* Nanoscale **7**, 6556 (2015) http://doi.org/10.1039/C5NR00205B.

[18] C. M. Ramsdale and N. C. Greenham, *Ellipsometric determination of anisotropic optical constants in electroluminescent conjugated polymers,* Adv. Mater. **14**, 212 (2002) http://doi.org/10.1002/1521-4095(20020205)14:3<212::AID-ADMA212>3.0.CO;2-V.

[19] X. Hong, T. Ishihara, and A. V. Nurmikko, *Dielectric confinement effect on excitons in PbI4-based layered semiconductors,* Phys. Rev. B **45**, 6961 (1992) http://doi.org/10.1103/PhysRevB.45.6961.

[20] D. Hu, X. Yang, C. Li, R. Liu, Z. Yao, H. Hu, S. N. G. Corder, J. Chen, Z. Sun, M. Liu, and Q. Dai, *Probing optical anisotropy of nanometer-thin van der waals microcrystals by near-field imaging,* Nat. Commun. **8**, (2017) http://doi.org/10.1038/s41467-017-01580-7.

[21] C. Zhang, M. Kohl, and D. Heitmann, *Effect of dielectric anisotropy of quantum wells on reflection,* Superlattices Microstruct. **5**, (1989).

[22] A. Fieramosca, L. De Marco, M. Passoni, L. Polimeno, A. Rizzo, B. L. T. Rosa, G. Cruciani, L. Dominici, M. De Giorgi, G. Gigli, L. C. Andreani, D. Gerace, D. Ballarini, and D. Sanvitto, *Tunable Out-of-Plane Excitons in 2D Single-Crystal Perovskites,* ACS Photonics **5**, 4179 (2018) http://doi.org/10.1021/acsphotonics.8b00984.

[23] B. Song, J. Hou, H. Wang, S. Sidhik, J. Miao, H. Gu, H. Zhang, S. Liu, Z. Fakhraai, J. Even, J. C. Blancon, A. D. Mohite, and D. Jariwala, *Determination of Dielectric Functions and Exciton Oscillator Strength of Two-Dimensional Hybrid Perovskites,* ACS Mater. Lett. 148 (2021) http://doi.org/10.1021/acsmaterialslett.0c00505.

[24] R. A. Decrescent, N. R. Venkatesan, C. J. Dahlman, R. M. Kennard, M. L. Chabinyc, and J. A. Schuller, *Optical Constants and Effective-Medium Origins of Large Optical Anisotropies in Layered Hybrid Organic/Inorganic Perovskites,* ACS Nano **13**, 10745 (2019) http://doi.org/10.1021/acsnano.9b05504.

[25] G. Walters, L. Haeberle, R. Quintero-bermudez, J. Brodeur, S. Kéna-Cohen, and E. H. Sargent, *Directional Light Emission from Layered Metal Halide Perovskite Crystals´,* J. Phys. Chem. Lett. **11**, (2020) http://doi.org/https://dx.doi.org/10.1021/acs.jpclett.0c00901.

[26] M. K. Jana, S. M. Janke, D. J. Dirkes, S. Dovletgeldi, C. Liu, X. Qin, K. Gundogdu, W. You, V. Blum, and D. B. Mitzi, *Direct-Bandgap 2D Silver-Bismuth Iodide Double Perovskite: The Structure-Directing Influence of an Oligothiophene Spacer Cation,* J. Am. Chem. Soc. **141**, 7955 (2019) http://doi.org/10.1021/jacs.9b02909.

[27] S. J. Hong, H. Chun, K. A. Min, and B. Han, *First-principles mechanism study on distinct optoelectronic properties of Cl-doped 2D hybrid tin iodide perovskite,* J. Mater. Chem. C **8**, 9540 (2020) http://doi.org/10.1039/d0tc01309a.

[28] J. Heyd, G. E. Scuseria, and M. Ernzerhof, *Erratum: Hybrid functionals based on a screened Coulomb potential (Journal of Chemical Physics (2003) 118 (8207)),* J. Chem. Phys. **124**, (2006) http://doi.org/10.1063/1.2204597.

[29] V. Blum, R. Gehrke, F. Hanke, P. Havu, V. Havu, X. Ren, K. Reuter, and M. Scheffler, *Ab initio molecular simulations with numeric atom-centered orbitals,* Comput. Phys. Commun. **180**, 2175 (2009) http://doi.org/10.1016/j.cpc.2009.06.022.

[30] S. V. Levchenko, X. Ren, J. Wieferink, R. Johanni, P. Rinke, V. Blum, and M. Scheffler, *Hybrid functionals for large periodic systems in an all-electron, numeric atom-centered basis framework,* Comput. Phys. Commun. **192**, 60 (2015) http://doi.org/10.1016/j.cpc.2015.02.021.

[31] W. P. Huhn and V. Blum, *One-hundred-three compound band-structure benchmark of post-self-consistent spin-orbit coupling treatments in density functional theory,* Phys. Rev. Mater. **1**, 1 (2017) http://doi.org/10.1103/PhysRevMaterials.1.033803.

[32] Y. Nagamune, S. Takeyama, and N. Miura, *Exciton spectra and anisotropic Zeeman effect in PbI2 at high magnetic fields up to 40 T,* Phys. Rev. B **43**, 12401 (1991) http://doi.org/10.1103/PhysRevB.43.12401.

[33] J. N. Hilfiker, N. Singh, T. Tiwald, D. Convey, S. M. Smith, J. H. Baker, and H. G. Tompkins, *Survey of methods to characterize thin absorbing films with Spectroscopic Ellipsometry,* Thin Solid Films **516**, 7979 (2008) http://doi.org/10.1016/j.tsf.2008.04.060.

[34] M. Campoy-Quiles, P. G. Etchegoin, and D. D. C. Bradley, *On the optical anisotropy of conjugated polymer thin films,* Phys. Rev. B - Condens. Matter Mater. Phys. **72**, 1 (2005) http://doi.org/10.1103/PhysRevB.72.045209.

[35] J. B. Bult, R. Crisp, C. L. Perkins, and J. L. Blackburn, *Role of dopants in long-range charge carrier transport for p-type and n-type graphene transparent conducting thin films,* ACS Nano **7**, 7251 (2013) http://doi.org/10.1021/nn402673z.

[36] J. P. Perdew, K. Burke, and M. Ernzerhof, *Generalized gradient approximation made simple,* Phys. Rev. Lett. **77**, 3865 (1996) http://doi.org/10.1103/PhysRevLett.77.3865.

[37] A. Tkatchenko and M. Scheffler, *Accurate molecular van der Waals interactions from ground-state electron density and free-atom reference data,* Phys. Rev. Lett. **102**, (2009) http://doi.org/10.1103/PhysRevLett.102.073005.

[38] C. Liu, W. Huhn, K. Z. Du, A. Vazquez-Mayagoitia, D. Dirkes, W. You, Y. Kanai, D. B. Mitzi, and V. Blum, *Tunable Semiconductors: Control over Carrier States and Excitations in Layered Hybrid Organic-Inorganic Perovskites,* Phys. Rev. Lett. **121**, 146401 (2018) http://doi.org/10.1103/PhysRevLett.121.146401.

[39] J. Heyd, G. E. Scuseria, and M. Ernzerhof, *Hybrid functionals based on a screened Coulomb potential,* J. Chem. Phys. **118**, 8207 (2003) http://doi.org/10.1063/1.1564060.

[40] A. V. Krukau, O. A. Vydrov, A. F. Izmaylov, and G. E. Scuseria, *Influence of the exchange screening parameter on the performance of screened hybrid functionals,* J. Chem. Phys. **125**, (2006) http://doi.org/10.1063/1.2404663.

[41] R. Zhao, V. W. Z. Yu, K. Zhang, Y. Xiao, Y. Zhang, and V. Blum, *Quasi-four-component method with numeric atom-centered orbitals for relativistic density functional simulations of molecules and solids,* Phys. Rev. B **103**, 1 (2021) http://doi.org/10.1103/PhysRevB.103.245144.

[42] J. Even, L. Pedesseau, J. M. Jancu, and C. Katan, *Importance of spin-orbit coupling in hybrid organic/inorganic perovskites for photovoltaic applications,* J. Phys. Chem. Lett. **4**, 2999 (2013) http://doi.org/10.1021/jz401532q.

[43] M. Kepenekian and J. Even, *Rashba and Dresselhaus Couplings in Halide Perovskites: Accomplishments and Opportunities for Spintronics and Spin-Orbitronics,* J. Phys. Chem. Lett. **8**,

3362 (2017) http://doi.org/10.1021/acs.jpclett.7b01015.

[44] J. Leveillee, C. Katan, L. Zhou, A. D. Mohite, J. Even, S. Tretiak, A. Schleife, and A. J. Neukirch, *Influence of π -conjugated cations and halogen substitution on the optoelectronic and excitonic properties of layered hybrid perovskites,* Phys. Rev. Mater. **2**, 1 (2018) http://doi.org/10.1103/PhysRevMaterials.2.105406.

[45] K. Z. Du, Q. Tu, X. Zhang, Q. Han, J. Liu, S. Zauscher, and D. B. Mitzi, *Two-Dimensional Lead(II) Halide-Based Hybrid Perovskites Templated by Acene Alkylamines: Crystal Structures, Optical Properties, and Piezoelectricity,* Inorg. Chem. **56**, 9291 (2017) http://doi.org/10.1021/acs.inorgchem.7b01094.

[46] N. Kitazawa, *Optical absorption and photoluminescence properties of Pb(I, Br)-based two-dimensional layered perovskite,* Japanese J. Appl. Physics, Part 1 Regul. Pap. Short Notes Rev. Pap. **36**, 2272 (1997) http://doi.org/10.1143/jjap.36.2272.

[47] B. Febriansyah, T. M. Koh, Y. Lekina, N. F. Jamaludin, A. Bruno, R. Ganguly, Z. X. Shen, S. G. Mhaisalkar, and J. England, *Improved Photovoltaic Efficiency and Amplified Photocurrent Generation in Mesoporous n = 1 Two-Dimensional Lead-Iodide Perovskite Solar Cells,* Chem. Mater. **31**, 890 (2019) http://doi.org/10.1021/acs.chemmater.8b04064.

[48] M. Era, S. Morimoto, T. Tsutsui, and S. Saito, *Organic-inorganic heterostructure electroluminescent device using a layered perovskite semiconductor (C6H5C2H 4NH3)2PbI4,* Appl. Phys. Lett. **65**, 676 (1994) http://doi.org/10.1063/1.112265.

[49] N. Kitazawa, M. Aono, and Y. Watanabe, *Temperature-dependent time-resolved photoluminescence of (C 6H 5C 2H 4NH 3) 2PbX 4 (X = Br and I),* Mater. Chem. Phys. **134**, 875 (2012) http://doi.org/10.1016/j.matchemphys.2012.03.083.

[50] S. Neutzner, F. Thouin, D. Cortecchia, A. Petrozza, C. Silva, and A. R. Srimath Kandada, *Exciton-polaron spectral structures in two-dimensional hybrid lead-halide perovskites,* Phys. Rev. Mater. **2**, 1 (2018) http://doi.org/10.1103/PhysRevMaterials.2.064605.

[51] Q. Zhang, L. Chu, F. Zhou, W. Ji, and G. Eda, *Excitonic Properties of Chemically Synthesized 2D Organic–Inorganic Hybrid Perovskite Nanosheets,* Adv. Mater. **30**, 1 (2018) http://doi.org/10.1002/adma.201704055.

[52] F. Fuchs, C. Rödl, A. Schleife, and F. Bechstedt, *Efficient O (N2) approach to solve the Bethe-Salpeter equation for excitonic bound states,* Phys. Rev. B - Condens. Matter Mater. Phys. **78**, 1 (2008) http://doi.org/10.1103/PhysRevB.78.085103.

[53] W. J. Yin, T. Shi, and Y. Yan, *Unique properties of halide perovskites as possible origins of the superior solar cell performance,* Adv. Mater. **26**, 4653 (2014) http://doi.org/10.1002/adma.201306281.

[54] T. Inagaki, *Absorption spectra of pure liquid benzene in the ultraviolet region,* J. Chem. Phys. **57**, 2526 (1972) http://doi.org/10.1063/1.1678619.

[55] T. Zhu, W. P. Huhn, G. C. Wessler, D. Shin, B. Saparov, D. B. Mitzi, and V. Blum, *I2-II-IV-VI4 (I = Cu, Ag; II = Sr, Ba; IV = Ge, Sn; VI = S, Se): Chalcogenides for Thin-Film Photovoltaics,* Chem. Mater. **29**, 7868 (2017) http://doi.org/10.1021/acs.chemmater.7b02638.

[56] L. Claudio Andreani, *Optical Transitions, Excitons, and Polaritons in Bulk and Low-Dimensional*

Semiconductor Structures, in *Confin. Electrons Photons New Phys. Appl.*, edited by E. Burstein and C. Weisbuch (Springer US, Boston, MA, 1995), pp. 57–112 http://doi.org/10.1007/978-1-4615-1963-8_3.

[57] J. Even, L. Pedesseau, M. A. Dupertuis, J. M. Jancu, and C. Katan, *Electronic model for self-assembled hybrid organic/perovskite semiconductors: Reverse band edge electronic states ordering and spin-orbit coupling,* Phys. Rev. B - Condens. Matter Mater. Phys. **86**, 3 (2012) http://doi.org/10.1103/PhysRevB.86.205301.

[58] P. C. Sercel, J. L. Lyons, D. Wickramaratne, R. Vaxenburg, N. Bernstein, and A. L. Efros, *Exciton Fine Structure in Perovskite Nanocrystals,* Nano Lett. **19**, 4068 (2019) http://doi.org/10.1021/acs.nanolett.9b01467.

[59] T. Kataoka, T. Kondo, R. Ito, S. Sasaki, K. Uchida, and N. Miura, *Magneto-optical study on the excitonic spectrum of (C6H13NH3)2PbI4,* Phys. B Phys. Condens. Matter **184**, 132 (1993) http://doi.org/10.1016/0921-4526(93)90336-5.

[60] K. Tanaka, T. Takahashi, T. Kondo, K. Umeda, K. Ema, T. Umebayashi, K. Asai, K. Uchida, and N. Miura, *Electronic and excitonic structures of inorganic-organic perovskite-type quantum-well crystal (C4H9NH3) 2PbBr4,* Japanese J. Appl. Physics, Part 1 Regul. Pap. Short Notes Rev. Pap. **44**, 5923 (2005) http://doi.org/10.1143/JJAP.44.5923.

[61] K. Ema, K. Umeda, M. Toda, C. Yajima, Y. Arai, H. Kunugita, D. Wolverson, and J. J. Davies, *Huge exchange energy and fine structure of excitons in an organic-inorganic quantum well material,* Phys. Rev. B - Condens. Matter Mater. Phys. **73**, 3 (2006) http://doi.org/10.1103/PhysRevB.73.241310.

[62] M. D. Smith, L. Pedesseau, M. Kepenekian, I. C. Smith, C. Katan, J. Even, and H. I. Karunadasa, *Decreasing the electronic confinement in layered perovskites through intercalation,* Chem. Sci. **8**, 1960 (2017) http://doi.org/10.1039/c6sc02848a.

[63] R. R. Guseinov, *Coulomb Interaction and Excitons in a Superlattice,* Phys. Status Solidi B **125**, 237 (1984) http://doi.org/10.1002/pssb.2221250128.

[64] M. Dyksik, S. Wang, W. Paritmongkol, D. K. Maude, W. A. Tisdale, M. Baranowski, and P. Plochocka, *Tuning the Excitonic Properties of the 2D (PEA)2(MA)n-1PbnI3 n+1Perovskite Family via Quantum Confinement,* J. Phys. Chem. Lett. **12**, 1638 (2021) http://doi.org/10.1021/acs.jpclett.0c03731.

[65] J. M. Luttinger, *Quantum theory of cyclotron resonance in semiconductors: General theory,* Phys. Rev. **102**, 1030 (1956) http://doi.org/10.1103/PhysRev.102.1030.

[66] M. Gramlich, M. W. Swift, C. Lampe, J. L. Lyons, M. Do¨blinger, A. L.Efros, P. C. Sercel, and A. S. Urban, *Dark and Bright Excitons in Halide Perovskite Nanoplatelets,* Adv. Sci. **Accepted**, (2021) http://doi.org/10.1002/ADVS.202103013.

[67] M. W. Swift, J. L. Lyons, A. L. Efros, and P. C. Sercel, *Rashba exciton in a 2D perovskite quantum dot,* Nanoscale **13**, 16769 (2021) http://doi.org/10.1039/d1nr04884h.

[68] C. Ambrosch-Draxl and J. O. Sofo, *Linear optical properties of solids within the full-potential linearized augmented planewave method,* Comput. Phys. Commun. **175**, 1 (2006) http://doi.org/10.1016/j.cpc.2006.03.005.

[69] S. M. Janke, M. B. Qarai, V. Blum, and F. C. Spano, *Frenkel-Holstein Hamiltonian applied to absorption spectra of quaterthiophene-based 2D hybrid organic-inorganic perovskites,* J. Chem. Phys. **152**, (2020) http://doi.org/10.1063/1.5139044.

[70] V. Havu, V. Blum, P. Havu, and M. Scheffler, *Efficient O (N) integration for all-electron electronic structure calculation using numeric basis functions,* J. Comput. Phys. **228**, 8367 (2009) http://doi.org/10.1016/j.jcp.2009.08.008.

[71] X. Ren, P. Rinke, V. Blum, J. Wieferink, A. Tkatchenko, A. Sanfilippo, K. Reuter, and M. Scheffler, *Resolution-of-identity approach to Hartree-Fock, hybrid density functionals, RPA, MP2 and GW with numeric atom-centered orbital basis functions,* New J. Phys. **14**, (2012) http://doi.org/10.1088/1367-2630/14/5/053020.

[72] F. Knuth, C. Carbogno, V. Atalla, V. Blum, and M. Scheffler, *All-electron formalism for total energy strain derivatives and stress tensor components for numeric atom-centered orbitals,* Comput. Phys. Commun. **190**, 33 (2015) http://doi.org/10.1016/j.cpc.2015.01.003.

[73] N. W. Ashcroft and N. D. Mermin, *Solid State Physics, Solid State Physics* (Thomson Learning, Philadelphia, 1976).

[74] J. S. Toll, *Causality and the dispersion relation: Logical foundations,* Phys. Rev. **104**, 1760 (1956) http://doi.org/10.1103/PhysRev.104.1760.

[75] C. Zhu, X. Yuan, F. Xiu, C. Zhang, Y. Xu, R. Zhang, Y. Shi, and F. Wang, *Broadband hot-carrier dynamics in three-dimensional Dirac semimetal Cd3As2,* Appl. Phys. Lett. **111**, 2 (2017) http://doi.org/10.1063/1.4985688.

[76] K. Momma and F. Izumi, *VESTA 3 for three-dimensional visualization of crystal, volumetric and morphology data,* J. Appl. Crystallogr. **44**, 1272 (2011) http://doi.org/10.1107/S0021889811038970.

[77] X. Chen, H. Lu, Z. Li, Y. Zhai, P. F. Ndione, J. J. Berry, K. Zhu, Y. Yang, and M. C. Beard, *Impact of Layer Thickness on the Charge Carrier and Spin Coherence Lifetime in Two-Dimensional Layered Perovskite Single Crystals,* ACS Energy Lett. **3**, 2273 (2018) http://doi.org/10.1021/acsenergylett.8b01315.

[78] B. Johs and J. S. Hale, *Dielectric function representation by B-splines,* Phys. Status Solidi Appl. Mater. Sci. **205**, 715 (2008) http://doi.org/10.1002/pssa.200777754.

[79] J. N. Hilfiker and T. Tiwald, *Dielectric Function Modeling,* in *Spectrosc. Ellipsom. Photovoltaics Vol. 1 Fundam. Princ. Sol. Cell Charact.*, edited by H. Fujiwara and R. W. Collins (Springer International Publishing, Cham, 2018), pp. 115–153 http://doi.org/10.1007/978-3-319-75377-5_5.